Steepest descent integration: A novel method for computing wavefields radiated from borehole sources

Yihe Xu[1], Baoshan Wang[1], and Tao Xu[2]

ABSTRACT

Borehole sources, including chemical explosives, air gun, water gun, and piezoelectric transducers in the borehole, generate seismic waves inside and outside the borehole. Modeling the wavefield is of key importance in acoustic logging, crosshole tomography, mining geophysics, and deep sounding seismic for interpretation of amplitude information of real data and prediction of energy-radiation patterns. Classic methods for modeling the wavefield inside a borehole, such as real-axis integration, are challenged by highly oscillatory integrals encountered when modeling the wavefield outside the borehole. We have developed a novel method, called steepest descent integration (SDI), which evaluates the oscillatory wavenumber integration by numerically integrating along the steepest descent path. The oscillation along the new integration path is significantly reduced. The contributions of poles and branch cuts are added if they are located between the steepest descent path and the real axis. The SDI is applicable to arbitrary frequency and source-receiver distance. Comparison with real-axis integration shows that the method can compute highly oscillatory integrals with better efficiency and accuracy. In addition, the SDI is more numerically robust because it generates no spurious arrivals, which are evident in the real-axis integration. Analysis of numerical examples at different source-receiver distance shows that SDI is more efficient when computing far-field seismograms. This SDI can also be used to compute highly oscillatory integral in other wave-propagation problems.

INTRODUCTION

Active source seismology is of extreme importance in identifying and locating hydrocarbon reservoirs and obtaining high-resolution images of the crust. The most common source model in active source seismology is the point-source model. However, numerous studies have proposed several new source models for better understanding of unusual arrivals and their amplitude information. Acoustic logging and crosshole tomography often enclose a point source with a fluid-filled borehole (Tsang and Rader, 1979; Kurkjian and Chang, 1986; Chen et al., 2014; Zheng et al., 2015), whereas deep-sounding seismic or mining geophysics studies replace the point-source model by stresses acting on a blast-hole wall (Heelan, 1953; Blair, 2007, 2010). The common modification of the new source models is the addition of a cylindrical hole around the sources, which significantly changes the radiation pattern and generates additional waves. They are therefore called downhole seismic sources or downhole sources.

In wavefield modeling of downhole seismic source problems, semianalytical methods have played an important role because of the ease of handling surface waves along the borehole wall and the accurate description of the effect of cylindrical boundaries on wavefields. Basically, a semianalytical method derives analytical solutions in the frequency-wavenumber domain and then transforms it back to the time-space domain using numerical methods. Although analytical solutions of borehole sources have been obtained for the empty borehole (Heelan, 1953) and fluid-filled borehole (Lee and Balch, 1982) in an isotropic medium (Tsang and Rader, 1979), transversely isotropic medium (He and Hu, 2009), porous medium (Rosenbaum, 1974), cracked porous medium (Tang et al., 2012), and for seismoelectric effects (Zheng et al., 2015), numerical methods for transforming analytical solutions back have

received less attention, especially for the propagation of elastic waves outside the borehole.

Numerical methods commonly used for computing the wavefield excited by borehole sources are real-axis integration (Tsang and Rader, 1979; Zheng et al., 2015), the discrete wavenumber method (Bouchon and Aki, 1977; Cheng and Toksöz, 1981), and branch-cut integration (Kurkjian, 1985; He and Hu, 2009; Chen et al., 2014). They all face challenges when computing far-field seismograms outside the borehole because of highly oscillatory integrals in wavenumber integration. The first two methods use sampling points on the real axis of the complex wavenumber plane to yield complete waveforms. The real-axis integration explicitly discretizes the wavenumber integral (Tubman et al., 1984; Zheng et al., 2015); whereas the discrete wavenumber method converts the wavenumber integral into summation by introducing evenly spaced virtual sources (White and Zechman, 1968; Bouchon and Aki, 1977). The integrand behaves like $\exp(iCk)$ on the real axis, where k is the wavenumber and C is a constant proportional to the source-receiver distance. Therefore, the integrand would become highly oscillatory when the source-receiver distance is large, reducing the accuracy of the numerical integration (Chen and Zhang, 2001). One possible solution is dense sampling. Yet, the rate of sampling must be carefully chosen because of the trade-off between efficiency and spurious signals caused by inadequate sampling (Bouchon, 2003).

The branch-cut integration provides an oscillation-free way to compute the wavefield when the receiver is located inside the borehole (Kurkjian, 1985; He and Hu, 2009; Chen et al., 2014). It deforms the integration path from the real axis to the branch cuts, which are nearly identical to the steepest descent path in the case
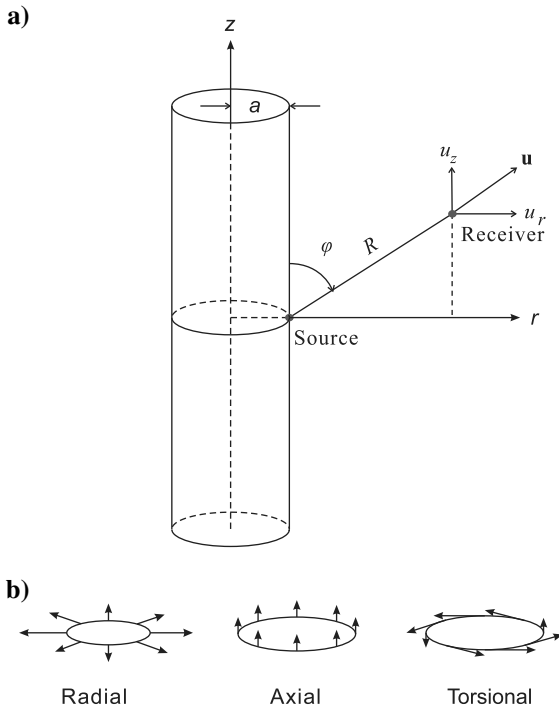
a)

b)

Figure 1. Illustration of downhole sources (modified after Xu et al., 2015). (a) Source geometry. The stress is axisymmetrically applied on the borehole wall with the radius of a. The receiver is located at point (r, z). Cylindrical coordinates are used for concise description of the problem. (b) Three basic types of downhole seismic sources.

of acoustic logging. The integrand behaves as $\exp(-X^2)$, where X is a real number varying from $-\infty$ to $+\infty$ along the path. Hence, it is an efficient method. However, when the receiver moves outside the borehole, the integrand will also become highly oscillatory again because the steepest descent path is no longer coincident with the branch cut.

Here, we propose a new numerical integration method by changing the integration path to the steepest descent path, which keeps the efficiency and flexibility of the branch-cut integration for computation of the far-field wavefield outside the borehole. Similar ideas have been commonly used in many fields associated with the evaluation of highly oscillatory integrals (Aki and Richards, 2002), often referred to as the method of steepest descent or the steepest descent method (SDM). The basic SDM approximates the steepest descent path with a single straight line and the integrand with its Taylor approximation. Despite that SDM has evolved (Khanh, 1995; López et al., 2009), it still uses the value of the integrand and/or its derivatives on several special points (i.e., saddle points) to approximate the whole integral. It is only accurate under certain conditions, such as in the far-field or at a high frequency. In our method, we use no approximations. The integrand is numerically integrated along the steepest descent path (Huybrechs and Vandewalle, 2006; Xu et al. 2015). Therefore, the method is more accurate than SDM and is applicable to near- and far-field cases. It is referred to as steepest descent integration (SDI) in this paper.

Although SDI is efficient and accurate, it has drawn little attention. There may be two reasons. On one hand, the classic SDM already has favorable accuracy in evaluating the far-field wavefield. On the other hand, implementation of SDI should deal with the tricky multivalued function around the saddle points (Huybrechs and Vandewalle, 2006). Recent studies show that asymptotic solutions of displacements derived by SDM are only valid in limited cases (Blair, 2007; Xu et al., 2015). A numerical solution is demanded for better prediction of wavefields, especially for the amplitude. In this paper, we solve the multivalued problem by considering Sommerfeld radiation condition and the analyticity of complex displacement functions. A comparison of the accuracy and efficiency between the SDI and the real-axis integration is also presented.

STEEPEST DESCENT INTEGRATION

Borehole source problem and its analytical solution in the frequency-wavenumber domain

Consider an empty borehole of radius a and infinite length embedded in an isotropic linear elastic medium. Borehole sources are represented by stresses on the borehole wall (Figure 1). The three basic types of borehole sources are radial, axial, and torsional sources. Without losing generality, we consider radial sources in this study. In a cylindrical coordinate system, an axisymmetric radial borehole sources can be written as

$$\sigma_{rr}|_{r=a} = \delta(z)G(t), \quad \sigma_{rz}|_{r=a} = \sigma_{r\theta}|_{r=a} = 0, \quad (1)$$

where $\sigma_{rr}, \sigma_{r\theta}, \sigma_{rz}$ are the stresses applied on the borehole wall, $\delta(z)$ is the Dirac delta function, and $G(t)$ is the source-time function. The displacements in the frequency-wavenumber domain can be obtained analytically (Heelan, 1953; Meredith, 1990; see Appendix A for a detailed derivation):

$$U_r(r, k_z, \omega) = \frac{k_r^{(c)}(\rho\omega^2 - 2\mu k_z^2)H_1^{(1)}(k_r^{(s)}a)}{D}G(\omega)H_1^{(1)}(k_r^{(c)}r)$$
$$+ \frac{2\mu k_r^{(c)}k_z^2 H_1^{(1)}(k_r^{(c)}a)}{D}G(\omega)H_1^{(1)}(k_r^{(s)}r),$$

$$U_z(r, k_z, \omega) = \frac{-ik_z(\rho\omega^2 - 2\mu k_z^2)H_1^{(1)}(k_r^{(s)}a)}{D}G(\omega)H_0^{(1)}(k_r^{(c)}r)$$
$$+ \frac{2i\mu k_z k_r^{(c)}k_r^{(s)}H_1^{(1)}(k_r^{(c)}a)}{D}G(\omega)H_0^{(1)}(k_r^{(s)}r),$$

$$(2)$$

where U_r, U_z are the radial and vertical component of displacements in the frequency-wavenumber domain; r and z are the position of the receiver; $k_r^{(c)}$ and $k_r^{(s)}$ are the radial wavenumber associated with the P- and S-waves; ρ, λ, μ are the density and Lamé parameters of the elastic medium; ω is the frequency; $G(\omega)$ is the Fourier transform of the source time function $G(t)$; and $H_n^{(m)}$ is the Hankel function. The values of $k_r^{(c)}$, $k_r^{(s)}$, and D are given by

$$k_r^{(c,s)} = (\omega^2/c^{(c,s)2} - k_z^2)^{1/2}, \tag{3}$$

$$D = (\rho\omega^2 - 2\mu k_z^2)^2 H_0^{(1)}(k_r^{(c)}a)H_1^{(1)}(k_r^{(s)}a)$$
$$+ 4\mu^2 k_z^2 k_r^{(c)}k_r^{(s)}H_1^{(1)}(k_r^{(c)}a)H_0^{(1)}(k_r^{(s)}a)$$
$$- 2\mu\rho\omega^2 k_r^{(c)}\frac{1}{a}H_1^{(1)}(k_r^{(c)}a)H_1^{(1)}(k_r^{(s)}a), \tag{4}$$

where $c^{(c,s)}$ is the velocity of the P- and S-waves. Then, their counterparts in the time-space domain are calculated via 2D numerical integration over the wavenumber and frequency (Meredith, 1990; Blair, 2007)

$$u_{r,z}(r, z, t)$$
$$= \left(\frac{1}{2\pi}\right)^2 \int_{-\infty}^{+\infty}\left(\int_{-\infty}^{+\infty} U_{r,z}(r, k_z, \omega)e^{ik_z z}dk_z\right)e^{-i\omega t}d\omega. \tag{5}$$

The outer integral of ω is commonly evaluated by the fast Fourier transform. The focus of this paper is to present an efficient method to compute the integral of k_z:

$$I_{r,z}(\omega) = \int_{-\infty}^{+\infty} U_{r,z}(r, k_z, \omega)e^{ik_z z}dk_z, \tag{6}$$

which is also known as wavenumber integration.

From the real axis to the steepest descent path

The first step to construct the SDI is deforming the integration path from the real axis to the steepest descent path. The integrand of the wavenumber integration, $U_{r,z}(r, \omega, k_z)\exp(ik_z z)$, is a summation of products of Hankel functions and exponential functions. Separating $U_{r,z}(r, \omega, k_z)\exp(ik_z z)$ into the $H_n^{(m)}(k_r^{(c)}r)$ part and the $H_n^{(m)}(k_r^{(s)}r)$ part, the oscillatory behavior of each part is controlled

by $\exp(i(k_r^{(c,s)}r + k_z z))$. Consequently, it is oscillatory along the real axis and becomes highly oscillatory when the source-receiver distance is large (Figure 2). Hence, the sampling rate of the real axis method and the discrete wavenumber method positively correlates to the source-receiver distance, which greatly reduces their efficiency in far-field cases.

Deforming the integration path to the steepest descent path can remove the oscillation (Figure 3). Each part of $U_{r,z}(r, \omega, k_z)\exp(ik_z z)$ can be written as a product of the oscillatory part $\exp(f(k_z))$ and the smooth part $F(k_z)$:

$$U_{rz}(r, \omega, k_z)\exp(ik_z z) = F^{(c)}(k_z)\exp(f^{(c)}(k_z))$$
$$+ F^{(s)}(k_z)\exp(f^{(s)}(k_z)),$$
$$f^{(c,s)}(k_z) = i(k_r^{(c,s)}r + k_z z). \tag{7}$$

The steepest descent path is then obtained by keeping the imaginary part of the exponential term $f(k_z)$ constant along the whole path (Aki and Richards, 2002):

$$f(k_z) = f(k_{zs}) - X^2, \tag{8}$$

where X is the arbitrary real number and k_{zs} is the saddle point determined by $f'(k_{zs}) = 0$. k_{zs} and $f(k_{zs})$ are

$$k_{zs} = \frac{\omega z}{cR}, \qquad f(k_{zs}) = i\frac{\omega R}{c}, \tag{9}$$

where $R(= [(r - a)^2 + z^2]^{1/2})$ is the source-receiver distance. Substituting equations 3 and 7 into equation 8, one can obtain a quadratic equation of k_z:
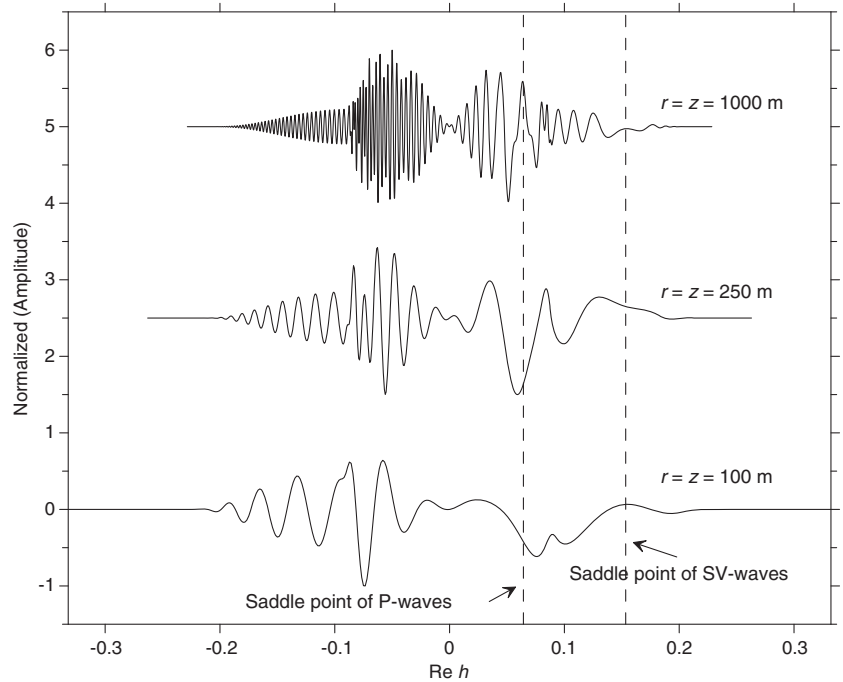

Figure 2. High oscillatory integrand due to the large source-receiver distance. The integrand of real-axis integration for receivers at three different distances is presented. The oscillation increases as the source-receiver distance increases. The high-oscillatory part requires dense sampling, but contributes little to the final integral.

$$R^2 k_z^2 + 2i[f(k_{zs}) - X^2]z k_z$$
$$- \{[f(k_{zs}) - X^2]^2 + \omega^2(r-a)^2/c^{(c,s)2}\} = 0. \quad (10)$$

It is the equation of the steepest descent path. Based on Cauchy's integral theorem in complex analysis, a contour integral is path-independent when the paths connect the same two points. Therefore, integrating along the steepest descent path and the real-axis path is identical if the contributions of poles and branch cuts are considered. Substituting equations 7 and 8 in equation 6, one can obtain

$$\int_{-\infty}^{+\infty} [F^{(c)}(k_z(X)) \exp(f^{(c)}(k_{zs})) k_z'(X)] \exp(-X^2) dX$$
$$+ \int_{-\infty}^{+\infty} [F^{(s)}(k_z(X)) \exp(f^{(s)}(k_{zs})) k_z'(X)] \exp(-X^2) dX.$$
$$(11)$$

It is then evaluated by the numerical integration method. Throughout the paper, we use two methods. When comparing the SDI with the real-axis method on accuracy and efficiency, we adopt the trapezoidal quadrature, which is straightforward for analysis. When computing the near-field synthetics, we adopt the adaptive Gauss-Kronrod quadrature instead (Press et al., 1992), which can easily deal with the singularity caused by poles in near-field cases. Given the form of equation 11, Gauss-Hermite quadrature could be a more efficient algorithm. However, because it is not adaptive, it can only be an alternative for far-field cases.

Multivalued functions

The trickiest issue is the multivalued function. The $U_{r,z}(r, \omega, k_z)$ has two values over the complex plane of k_z due to the square-root function appears when calculating radial wavenumber k_r:

$$k_r(k_z) = (\omega^2/c^{(c,s,f)2} - k_z^2)^{\frac{1}{2}}. \quad (12)$$

In conventional real-axis integration, the Sommerfeld radiation condition is used to select the physically meaningful value provided that no incoming wave exists (Meredith, 1990), resulting in a single-valued integration path. In the branch-cut method, the single-valued path is determined by analytically deforming the path in real-axis integration to the branch cut (He and Hu, 2009). SDI adopts a similar method to determine the value on the integration path, i.e., by analytically deforming the path in real-axis integration to the steepest descent path. During the deformation, if the integration path sweeps across a branch point, k_r changes its sign and an additional contribution of a contour around the branch cut is involved in the integration; if it sweeps across a pole, a closed contour circling the pole is added.
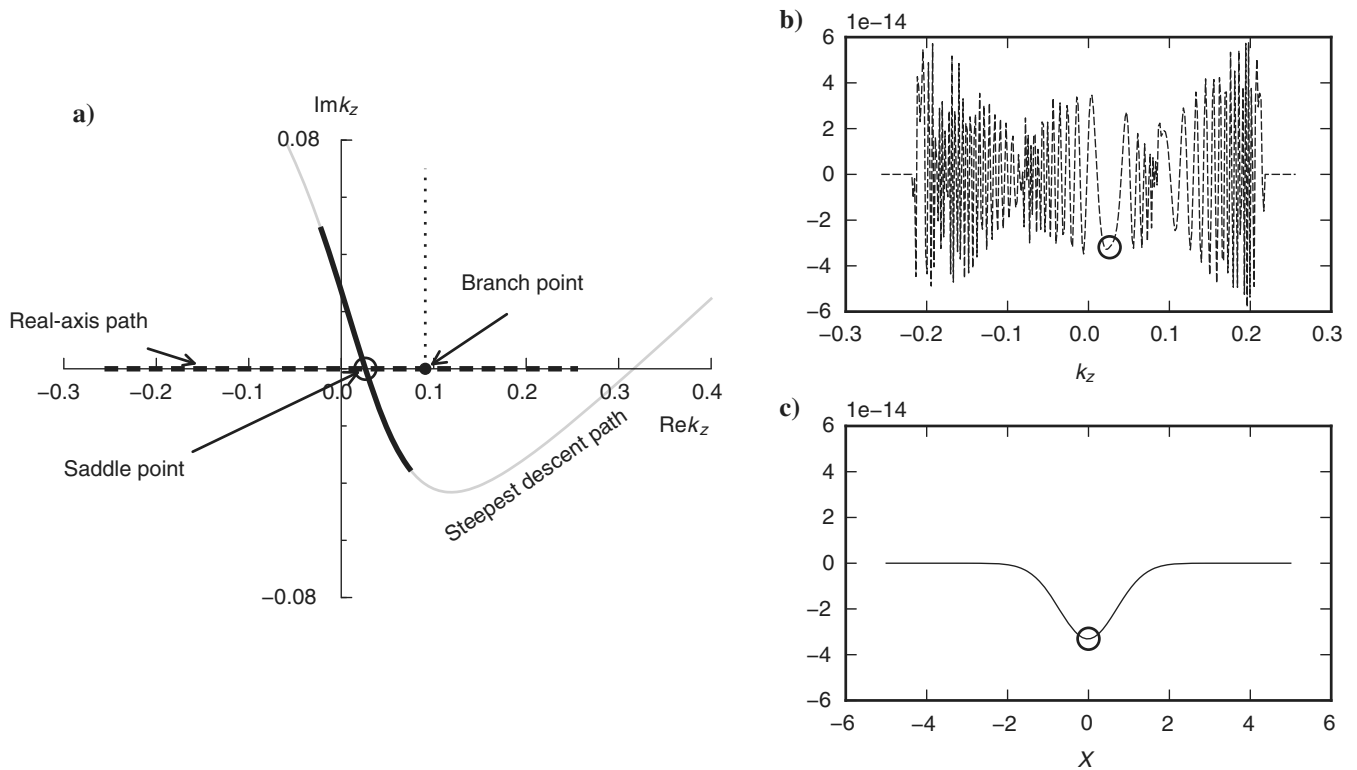

Figure 3. SDI. This figure shows an example of SDI and its comparison with real-axis integration. (a) The integration path of SDI (solid line) and the real-axis integration (dashed line) used in computation. A thin gray line is used to show a more complete steepest descent path. The saddle point is denoted by a circle, and the branch point is denoted by a dot. The vertical dotted line connected to the branch point is one choice of branch cut. (b) The integrand of real-axis integration (real part of the radial component). The circle marks the value corresponding to the saddle point. The integrand is highly oscillatory except in the vicinity of saddle points. (c) The integrand of SDI (the real part of the radial component of the P-wave). The circle marks the value corresponding to the saddle point. The integrand is smooth and decays extremely quickly.

The integration path of the SDI deforms along with the location of receivers; then, obtaining the single-valued path is more complicated than the real-axis method and the branch-cut method, which deal with a fixed integration path (Figure 4a). To simplify the strategy of choosing the radial wavenumber, we analyze all the possible conditions and categorize them to three different types. For each type, we choose a branch cut that has no intersection with the steepest descent path. Figure 4 shows an example of $\omega > 0$ and $z > 0$. The path intersects the real axis in two points, k_1 and k_2. The term k_1 is the saddle point k_{zs} in equation 9, and $k_2 = \omega R / c^{(c,s,f)} z$. If the branch point $k_c = \omega / c^{(c,s,f)}$ is smaller than both the two points, the branch cut in Figure 4b is chosen. If k_c is between the two points, the vertical branch cut is chosen (Figure 4c).

If k_c is larger than both the two points, the branch cut in Figure 4d is chosen. Figure 4e and 4f illustrates two variants of the second type.

In numerical implementation, the detailed strategy is slightly modified for simplicity and robustness. The square-root function provided by most numerical libraries has a branch cut like the one shown in Figure 4d. Because the square-root function is a two-valued function, this branch cut provides two single-valued function. The Sommerfeld cut also provides two single-valued functions (He and Hu, 2009). Then, we have four single-valued functions of the square-root function in total. Splitting the steepest descent path into two segments at the saddle point by setting $X > 0$ and $X < 0$, the integrand on each segment is computed by one of the
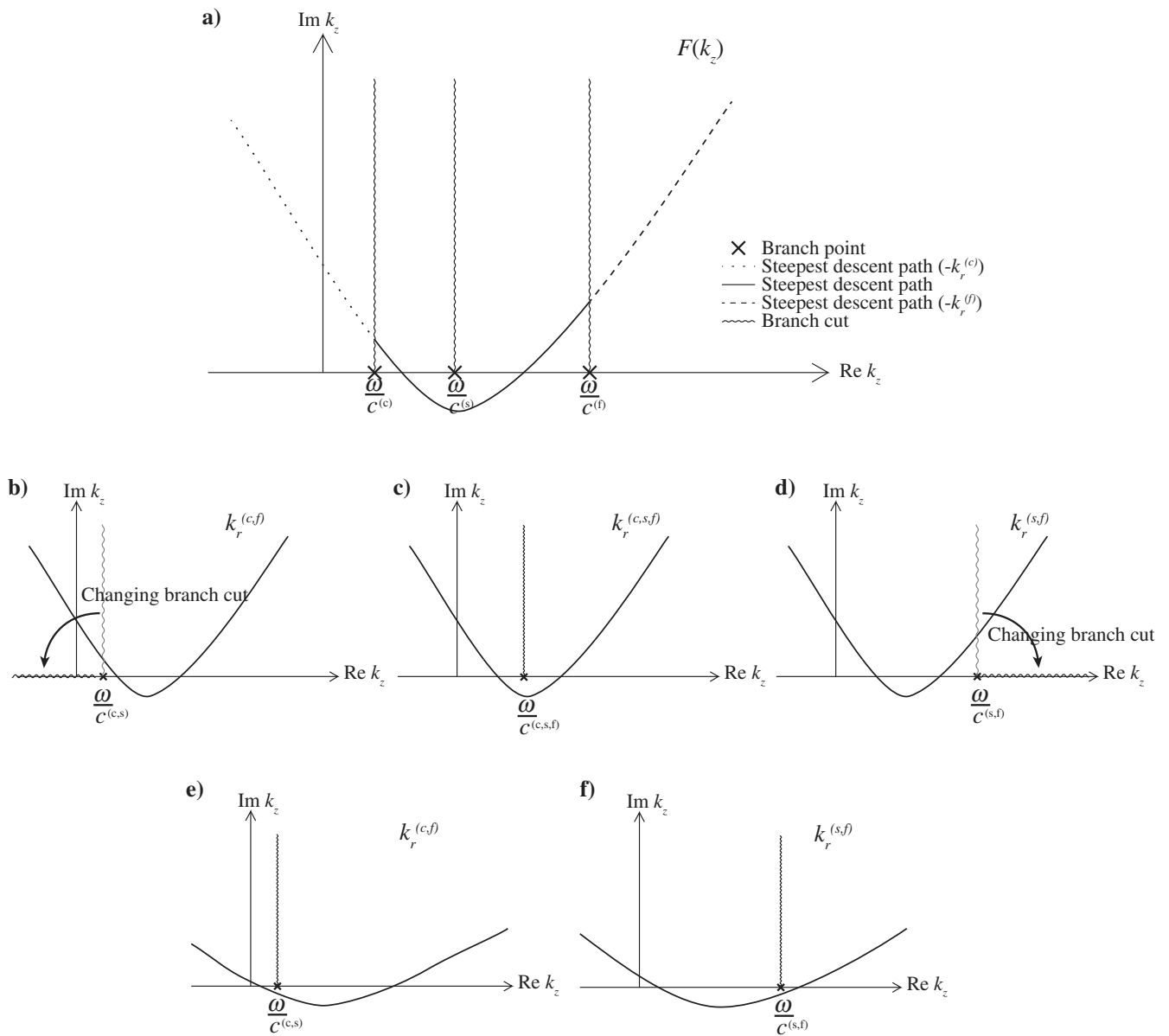

Figure 4. Sketch map of constructing a single-valued function of k_r. (a) Steepest descent path and value changes of k_r along the path. (b-d) are the three different conditions and the corresponding strategy for obtaining a single-valued k_r. (e and f) The two variants of condition (c), and they use the same strategy as (c).

four single-valued functions, according to the frequency ω, vertical distance z. The detailed strategy is described in Table 1.

The multivalued Hankel functions $H_n^{(1,2)}(k_r r)$ are another issue because the numerical libraries only provide routines to compute one single-valued function. The single-valued function corresponds to $-\pi < \text{Arg } k_r \leq \pi$, which is adequate for real-axis integration. However, SDI requires $H_n^{(1,2)}(k_r r)$ analytic on $-\pi < \text{Arg} k_r \leq 1.5\pi$. To tackle this issue, we utilize the relationship between the $H_n^{(1)}(k_r r)$ and $H_n^{(2)}(k_r r)$, to extend the analytic domain of $H_n^{(1)}(k_r r)$ to $-\pi < \text{Arg } k_r \leq 2\pi$ (Gradshteyn and Ryzhik, 2007):

$$H_n^{(1)}(k_r r) = \begin{cases} H_n^{(1)}(k_r r), & -\pi < \text{Arg } k_r \leq \pi, \\ \exp(i\pi n)H_n^{(2)}(k_r r \exp(-i\pi)), & \pi < \text{Arg } k_r \leq 2\pi. \end{cases} \tag{13}$$

COMPARISON WITH ANALYTICAL ASYMPTOTIC SOLUTIONS

Before comparing with the real-axis integration, SDI is first validated by comparing with the far-field analytical asymptotic solutions (Heelan, 1953). SDI is applicable to all source-receiver distance and any frequency, whereas asymptotic solutions are accurate only when $|k_r a|$ is small and $|k_r r|$ is large, called the Heelan regime in Blair (2007). Thus, the comparison in this subsection is constrained in the Heelan regime.

In the following examples, the velocities of P- and S-waves of the solid medium are 2074 and 869 m/s, respectively. The typical value of the borehole radius is 0.1 m (Tubman et al., 1984). A source with a peak frequency of 30 Hz is used. The receiver is at $r = 1000$ m, $z = 0$ m. The term k_r depends on frequency f, velocity c, and take-off angle:

$$k_r = \frac{2\pi f}{c} \cos \phi. \tag{14}$$

These parameters result in wavenumbers of 0.09 and 0.22 for the P- and S-waves respectively, satisfying the small $|k_r a|$ and large $|k_r r|$ conditions:

$$|k_r a| \leq |ka| = 0.022 \ll 1, \qquad |k_r r| = 90 \gg 1. \tag{15}$$

The source is a radial stress acting on the borehole wall, and two kinds of source time functions are tested. The first one is a Ricker wavelet, which is commonly used in waveform modeling in exploration seismology (Figure 5a):

$$\sigma_{rr}(r,t)|_{r=a} = \begin{cases} \delta(z)[1 - 2\pi^2 f_m^2(t-t_c)^2]\exp(-\pi^2 f_m^2(t-t_c)^2), & \text{if } 0 \leq t \leq 2t_c, \\ 0, & \text{otherwise,} \end{cases} \tag{16}$$

where σ_{rr} is the radial stress, $\delta(z)$ is the delta function, f_m is the peak frequency of the Ricker wavelet. The wavelet is truncated at $\pm t_c = 1/f_m = 1/30$ s and delayed t_c. Hence, the source starts at time 0 and lasts for $2t_c$. A time window $[R/c^{(c)} - t_c, R/c^{(s)} + 3t_c]$ is used to cover the P- and S-waves, where $c^{(c,s)}$ are the velocity of P- and S-waves, respectively. The second one is a more realistic function (Blair, 2007; Figure 5b):

$$\sigma_{rr}(r,t)|_{r=a} = \delta(z)P_{\text{VN}}(e\gamma/n)^n H(t)t^n e^{-\gamma t}, \tag{17}$$

where P_{VN} is the von Neumann borehole pressure, $H(t)$ the Heaviside unit-step function, γ a pressure decay parameter, and n an empirical integer. We use $\gamma = 1000$, $n = 6$ in this example.

Excellent agreement is found between the synthetic seismograms generated by SDI and the analytical asymptotic solutions for both source-time functions. It supports the validity of the SDI under the Heelan conditions (Blair, 2007), which is a necessary condition for the general validity.

COMPARSION WITH REAL-AXIS INTEGRATION

Accuracy comparison in the far-field

We compare the accuracy of the real-axis integration and SDI in two aspects. First, we analyze the general characteristics of their accuracy by comparing the root-mean-square (rms) errors of the

Table 1. Strategies for obtaining a single-valued function k_r. Denote $K = \text{sqrt}(\omega/c^2 - k_z^2)$, $\text{Re } K \geq 0$ is the value directly provided by numerical libraries. Three other single-valued functions can be constructed by $-K$ if $\text{Im } K > 0$, $-K$ if $\text{Im } K < 0$ and $-K$. We denote the four functions as 0, 1, 2, and 3. The singled-valued function can be obtained as follows. First, determine the possible strategies according to Table (a). Then, if the number of possible strategies is larger than one, choose the right one based on the relationship between the branch point k_c and the intersection points of the steepest descent path and the real axis k_1, k_2 (Tables b-d). L, R denote the left and right segments of the steepest descent path, respectively.

(a) Possible strategies for choosing k_r

Steepest descent path		P			S	
Horizontal wavenumber		$k_r^{(c)}$	$k_r^{(s,f)}$	$k_r^{(s)}$	$k_r^{(c,f)}$	
Strategies		I	I, II, III	I	I, II, III	

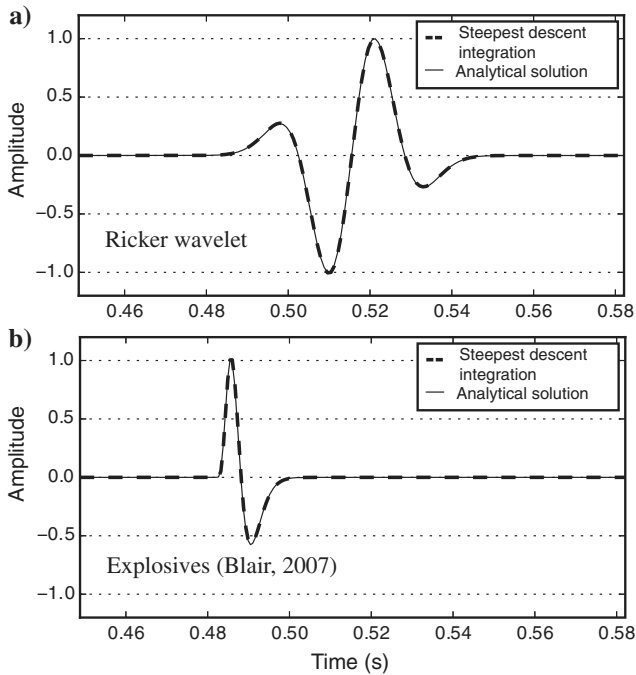| (b) I, $|k_1| < |k_c| < |k_2|$		L	R	(c) II, $|k_c| < |k_1| < |k_2|$		L	R	(d) III, $|k_1| < |k_2| < |k_c|$		L	R
$z \geq 0$	$\omega > 0$	0	1	$z > 0$	$\omega > 0$	3	1	$z > 0$	$\omega > 0$		0
	$\omega < 0$	2	0		$\omega < 0$	2	3		$\omega < 0$		
$z < 0$	$\omega > 0$	1	0	$z < 0$	$\omega > 0$	1	3	$z < 0$	$\omega > 0$		
	$\omega < 0$	0	2		$\omega < 0$	3	2		$\omega < 0$		

a)

b)

Figure 5. Comparison of a synthetic seismogram (dashed) with the analytical solution (solid) in the far-field using (a) the Ricker wavelet and (b) a more realistic wavelet (Blair, 2007). The synthetic seismogram is computed by SDI. The analytical solutions are obtained by Heelan (1953) using asymptotic analysis. They both are normalized by the maximum amplitude of the analytical solution; thus, the relative ratio between the amplitude of synthetic and analytical solutions is retained.

synthetic seismograms. The rms errors are measured by the rms of the difference between the synthetic seismograms and the analytical asymptotic solutions. Then, the detailed features of the seismograms are compared to study the spurious arrivals caused by spatial aliasing.

The synthetic seismograms at $r = 1000$ m, $z = 200$ m are generated using the same parameters as the ones in the last section (Figure 6a and 6b). Changing z from 0 to 200 m adds S-waves to the seismograms. We compute seismograms with different numbers of sampling points N for wavenumber integration. The range of N tested is from 3 to 1000. The sampling in the frequency integration stays unchanged through the following examples. Several representative examples are shown in Figure 6a and 6b. Two basic observation are that (1) the SDI needs much fewer sampling points ($N = 10$) than the real-axis integration ($N = 1000$) to obtain a good result, implying that SDI is more accurate and (2) the seismograms generated by real-axis integration have significant spurious arrivals when N is small, whereas those of SDI do not.

The rms errors, which are normalized by the peak amplitude of the analytical solutions, are plotted against the number of sampling points N. A positive correlation between the normalized rms errors and N is observed before N exceeds a certain limit of N_{min} (Figure 6c). The N_{min} are approximately 10 for SDI and 500 for real-axis integration in this example. Again, we find that SDI reaches maximum accuracy with fewer sampling points, i.e., 2% of the number of sampling points that the real-axis integration needs. Therefore, SDI has much higher accuracy.

To examine the spurious arrivals more closely, we zoom in on a short period just before the S arrivals (Figure 7). The bottom two seismograms are generated with extremely large N, regarded as the references. The eight seismograms above demonstrate the changes of seismograms as N increases. The spurious arrivals are evident in
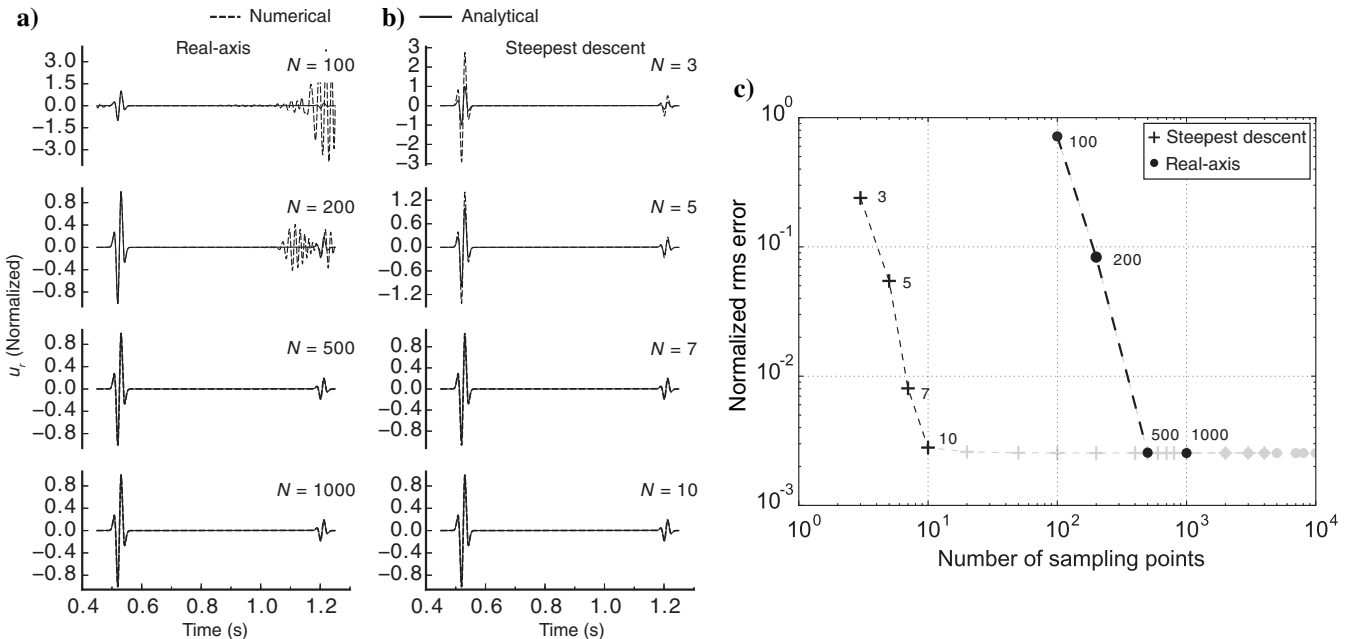

Figure 6. Synthetic seismograms of a different number of sampling points N for (a) real-axis integration and (b) SDI and their accuracy (c). Synthetics are dashed lines. The analytical solution (solid line) is used as a reference. Seismograms are normalized with respect to the maximum amplitude of the analytical solution. The accuracy in (c) is measured by normalized rms errors of numerical results. The rms errors of the SDI are denoted by crosses, and the real-axis integration is denoted by dots. Results are colored gray when the rms error stops decreasing.

the left four seismograms, which are computed by real-axis integration, until N reaches approximately 3000. In contrast, no spurious arrival exists in the seismograms generated by SDI, even with as small as seven sampling points. Therefore, SDI is also more accurate in terms of spurious arrivals. The spurious-arrival-free feature is of extreme importance in identifying signals and interpreting results when the signal-to-noise ratio is low or complex structures are involved.
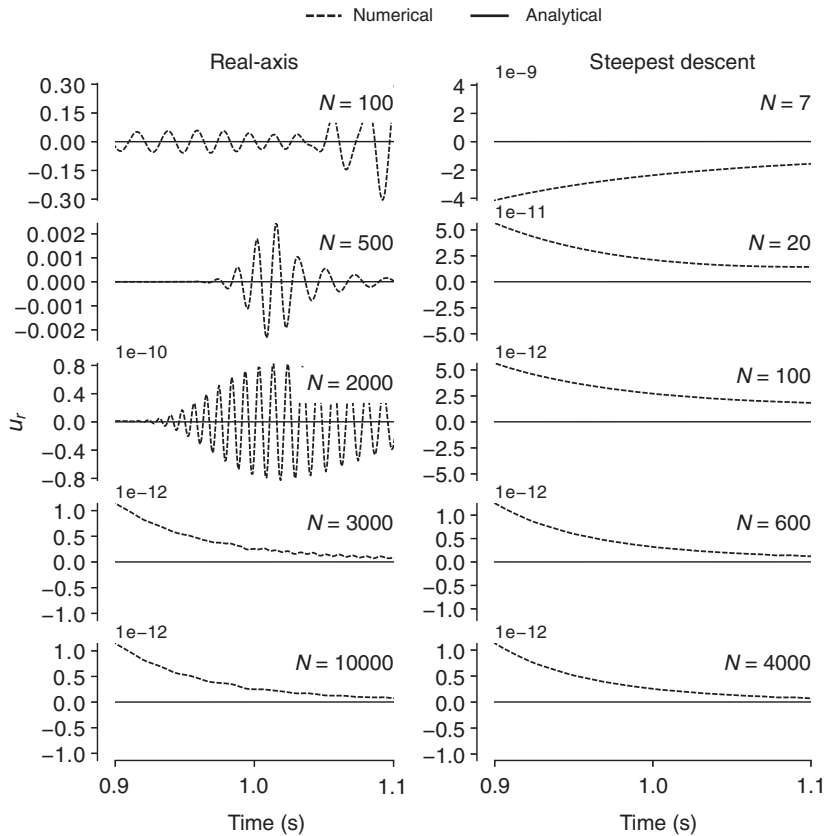

Figure 7. Magnification of the synthetic seismograms shown in Figure 5a and 5b in (0.9, 1.1 s). Numerical results are denoted by dashed lines, and analytical solutions are denoted by solid lines. Both are normalized by the maximum amplitude of the analytical solution in Figure 5a and 5b. The analytical solutions are extremely close to zero and appear as straight lines on the x-axis, so we have removed the x-axis in all subfigures. The real-axis integration and SDI present similar results with a large N. Spurious arrivals are evident in the results of the real-axis integration until $N \geq 3000$, whereas no spurious arrivals appear in synthetics of SDI.
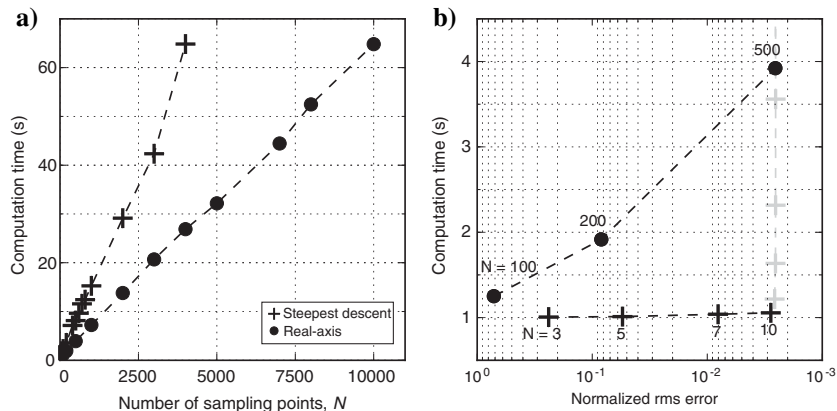

Figure 8. Comparison on computation time. Computation times of SDI (crosses) and real-axis integration (dots) are compared with respect to (a) the number of sampling points and (b) the normalized rms error. SDI is less efficient when using the same number of sampling points, however, when it costs less time to achieve the same accuracy.

Efficiency comparison in the far-field

The efficiency of the SDI and the real-axis integration are compared on a laptop with Intel Core i7-4712HQ. The two methods are both implemented in MATLAB. Comparing the computation time with respect to the same N shows that the SDI is less efficient (Figure 8a). The extra time is due to computing the steepest descent path and dealing with the multivalued functions. Nevertheless, SDI is more efficient with respect to the same accuracy (Figure 8b) because it needs a much lower N to reach a certain accuracy, which significantly reduces the overall computation time. When reaching maximum accuracy, SDI costs 1.06 s with 10 sampling points, whereas the real-axis integration costs nearly three times as much, i.e., 3.92 s, with $N = 500$. Therefore, despite the additional computation, SDI is still more efficient than real-axis integration in terms of the same accuracy.

Comparison of high-frequency near-field seismograms

The near-field case is necessary to demonstrate that SDI is applicable to all domains of R. It is more complicated for SDI than the far-field case because the influence of local characteristics of the integrand becomes evident. The pole's contribution is also more evident. To evaluate the wavenumber integration accurately, we use the adaptive Gauss-Kronrod rule instead of the simple trapezoidal rule. The seismograms at $r = 1$, $z = 0$ is calculated for 500, 1000, 2000, and 5000 Hz Ricker wavelets by SDI, the real-axis method, and asymptotic solutions. They are compared in Figure 8 to show that the seismograms by SDI and real-axis method are very close, which is a cross-validation of both methods. A significant difference from the far-field examples is that asymptotic solutions are no longer accurate even for small $|z/r|$ (Figure 9).

Dependence of computation time on source-receiver distance

Heretofore, we have been found that SDI can generate correct synthetic seismograms for the near- and far-fields, and it is advantageous regarding accuracy and efficiency in the far-field. Whether this efficiency remains for the near-field is still an open question. In this example, we compute seismograms for varied source-receiver

distance, from 1 to 5000 m. To reduce the bias introduced by the choice of sampling points, the number of sampling points N is set to $N_{\min}$ for each distance (Table 2). For real-axis integration, the $N_{\min}$ increases as R increases; whereas for SDI, the $N_{\min}$ approximately remains constant. Closer examination shows a slightly decreasing trend of the $N_{\min}$ as R increases for SDI (supplementary information that can be accessed through the following link: Figure S1).

The computation time for different source-receiver distances are thus obtained (Figure 10). The computation times of both methods have a positive relationship with R, while when increasing the rate of SDI, it is smaller. SDI is generally faster than the real-axis method despite that the real-axis method is slightly faster in the near-field. Therefore, SDI becomes slightly less efficient than the real-axis method in the near-field. However, it still has advantages in being free of spurious arrivals and the individual handling of different arrivals.

Effects of truncation and discretization of wavenumber integration on comparison

Truncation and discretization of the infinite wavenumber integral affect the precision and computation time of SDI and real-axis integration, which may introduce bias in the comparison. Generally, a large truncation or a small sampling interval gives better precision and a longer computation time. A proper truncation should be the minimum truncation that guarantees sufficient accuracy. A proper sampling interval should be the maximum interval that guarantees sufficient accuracy. For a given dominant frequency of the source and source-receiver distance, the proper truncation and sampling intervals depend on the desired accuracy. The most straightforward method to determine them is trial and error. Synthetic seismograms are computed for different truncations and sampling intervals using the two methods, and their accuracy is measured by the normalized rms errors (Figure 11). The general trend is that the rms error reduces when the truncation increases and the sampling interval shrinks. The rms error stops reduction when the truncation and the sampling interval reach certain thresholds. For real-axis integration, the threshold of truncation h_c is approximately 0.8 times the wavenumber of S-waves, $|\omega|/c_s$, and the threshold of the sampling intervals is slightly larger than $2\pi/L$, the criterion suggested by Bouchon (1981). For SDI, the thresholds are approximately 2.5 and 0.5, respectively.

The proper truncation and sampling intervals of real-axis integration are frequency dependent. Determining the truncation by evaluating the rms error for each frequency is computationally expensive. In this study, we adaptively determine the truncation using the properties of the integrand. The integrand decays as $\exp(-i\,\mathrm{Im}\,k_r(r-a))$, when $k_r > |\omega|/c_s$, then the integration could be truncated when $\exp(-i\,\mathrm{Im}k_r(r-a))$ is smaller than a given threshold ε. The truncation is then

$$k_c = \frac{1}{r-a}\log\left(\frac{1}{\varepsilon}\right) + \frac{|\omega|}{c^{(s)}}. \tag{18}$$

The threshold ε is set to an empirical value, 10^{-17}, which is applicable to all the examples in this study. Then, when computing a seismogram, the truncation positively correlates to the frequency (Figure 11a).

Conversely, the proper truncation and sampling intervals of the SDI are frequency independent because the effect of frequency is included in parameter X. The reason is that we set $f(k_z) = i(k_r^{(c,s)}r + k_z z)$ instead of $i(s_r^{(c,s)}r + s_z z)$, where $s_r^{(c,s)}$ is the slowness and $\omega s_r^{(c,s)} = k_r^{(c,s)}$. Then, the integrand along the SDP behaves like $\exp(-X^2)$ instead of $\exp(-\omega X^2)$. Therefore, determining the truncation and sampling intervals is irrelevant with the frequency. From Figure 11b, $X_c = 2$ and $\Delta X = 0.5$ could be the proper choice. However, we have adopted stricter parameters for all the numerical examples, i.e., $X_c = 5$ and $\Delta X = 0.5$, to guarantee the validity of the comparison results.

Comparison of truncation and discretization reveals that SDI gains no advantage by choosing parameters throughout compari-
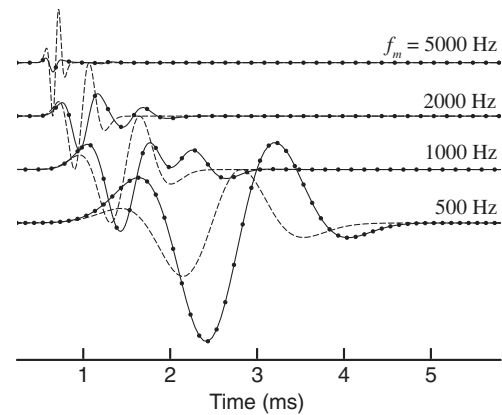

Figure 9. High-frequency waveforms in the near-field ($r = 1$, $z = 0$). The synthetics calculated by SDI and the real-axis method are denoted by solid lines and dots. The analytical solutions are denoted by dashed lines. All of the seismograms are normalized by the analytical solutions. The seismograms of the real-axis method are down-sampled to clearly show the solid lines under the dots.

Table 2. The $N_{\min}$ for different source-receiver distance R. For each R, the rms errors are evaluated at a different number of sampling points N. The $N_{\min}$ is the value when the rms error stops decreasing. For real-axis integration, the rms errors are evaluated at $N = 10, 20, 50, 100, 200, 500, 1000, 2000, 5000,$ and 10,000; for SDI, the rms errors are evaluated at $N = 3, 5, 10, 20, 50, 100, 200, 300, 400,$ and 800.

	$N_{\min}$	
$R(m)$	Real-axis	Steepest descent
1	50	10
10	50	10
20	100	10
50	100	10
100	200	10
200	200	10
500	500	10
1000	500	10
2000	1000	10
5000	5000	10

sons in this paper. Moreover, it has a simpler and more robust strategy for determining the proper truncation and sampling intervals. If replacing $X_c = 5$ by $X_c = 2$, the SDI could cost less computation time without losing too much accuracy.
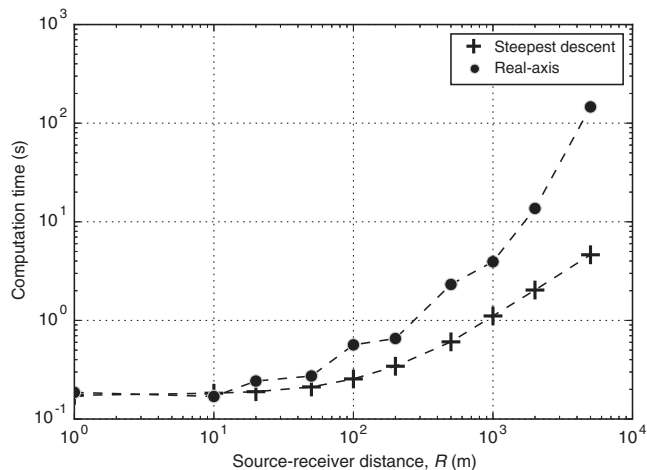

Figure 10. Increase of computation time for increasing R. The computation times are evaluated using the parameters in Table 2. SDI (crosses) is much more efficient in the far-field, whereas the real-axis integration (dots) has advantages in the near-field.

APPLICATION TO MODELING MACH WAVES

To test the validity of our method in the near-field case, we compute the wavefield excited by a point source in a fluid-filled borehole. The wavefield outside the borehole is dominated by the P-wave, S-wave, and tube wave. If the S-wave is slower than the tube wave, the tube wave will generate a secondary S-wave, named the Mach wave, whose characteristics are similar to shock waves in fluid mechanics (Meredith et al., 1993). Mathematically, this interesting phenomenon relates to the tube-wave pole, which moves close to the branch point and influences the integral. Unlike the real-axis method, SDI needs to include the pole's contribution explicitly. The pole is located numerically by the bisection method for each frequency. The searching bounds are set empirically to $[0.8\omega/c^{(s)}, 1.5\omega/c^{(s)}]$. The branch point $\omega/c^{(s)}$ is excluded from the search area to avoid numerical overflow. The pole's contribution is calculated by integrating along a small square enclosing the pole by the adaptive Gauss-Kronrod quadrature. The contribution is added if the pole is located between the steepest descent path and the real axis.

We use the Pierre shale as the solid medium (Meredith et al., 1993). The source is an explosive point source with a 100 Hz Ricker wavelet. The radial and vertical displacements are calculated on a 50×50 m grid with 0.5 m intervals. The source is placed at the origin. The vertical displacements at 40 ms is plotted (Figure 12). The convex wavefronts of the P- and S-waves are evident in the
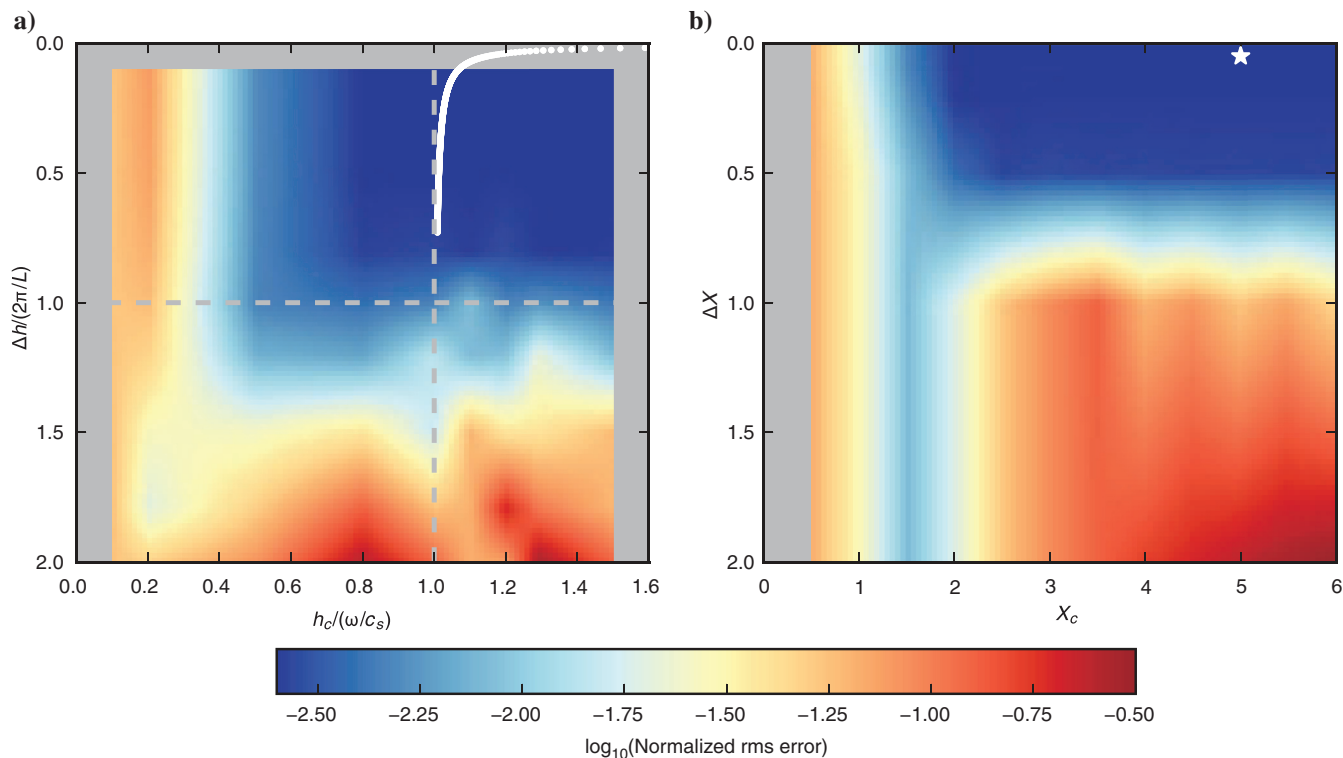

Figure 11. The rms error diagram of (a) the real-axis integration and (b) SDI. The normalized rms errors are shown in log scale. (a) The h_c and Δh are truncation and sampling intervals of the real-axis integration. The rms error is small when using large truncation and small sampling intervals. The series of white dots are automatically determined when computing seismograms using $N = 500$, each corresponding to an individual frequency. (b) The X_c and ΔX are truncation and sampling intervals of SDI, and the white star is the parameters in this study, applicable to an arbitrary frequency.
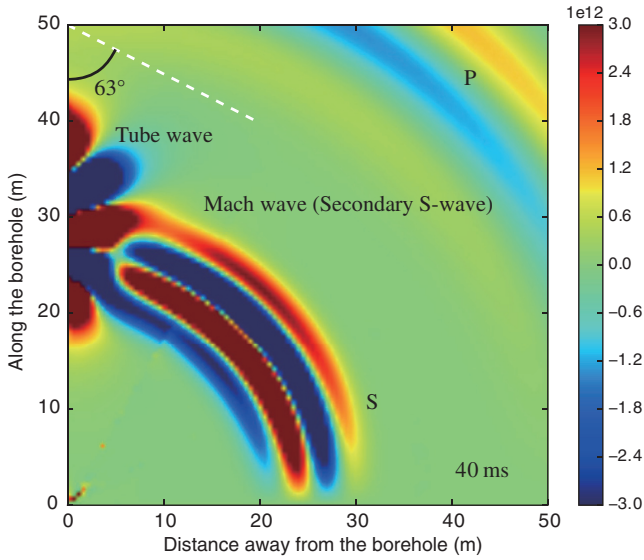
Figure 12. Snapshot of vertical displacement generated by a point source in fluid-filled borehole. The S-wave velocity in the solid medium is slower than the tube waves, and the Mach wave appears.

snapshot. A high-amplitude tube wave is traveling along the vertical borehole. If the S-wave is faster than the tube wave, they are decoupled. However, when the tube wave is faster (as in our case), a straight wavefront connects the tube wave and the S-wave. The angle between the wavefront and the borehole wall is 63°, which is identical to the Mach wave example in Meredith et al. (1993).

APPLICATION TO REAL DATA FROM BOREHOLE AIR-GUN SOURCE

To test the validity of our method in the far-field case, we compare the synthetic seismograms to real seismic records from a borehole air-gun project operated at Xundian, Yunnan Province, China (Yang et al., 2016). The diameter and depth of the borehole are 0.2 and 50 m, respectively. The water level in this borehole is −28 m. An air gun with the volume of 250 in³ is deployed 12 m below the water level. The air gun fires once per 30 min, and the seismic waves it generates are recorded by eight stations within the 1000 m (Figure 13). The velocity model is the same as the ones in the examples above. We compute synthetic seismograms using borehole monopole source model. Instead of directly comparing the waveforms, we compare the variations of the peak envelope ampli-
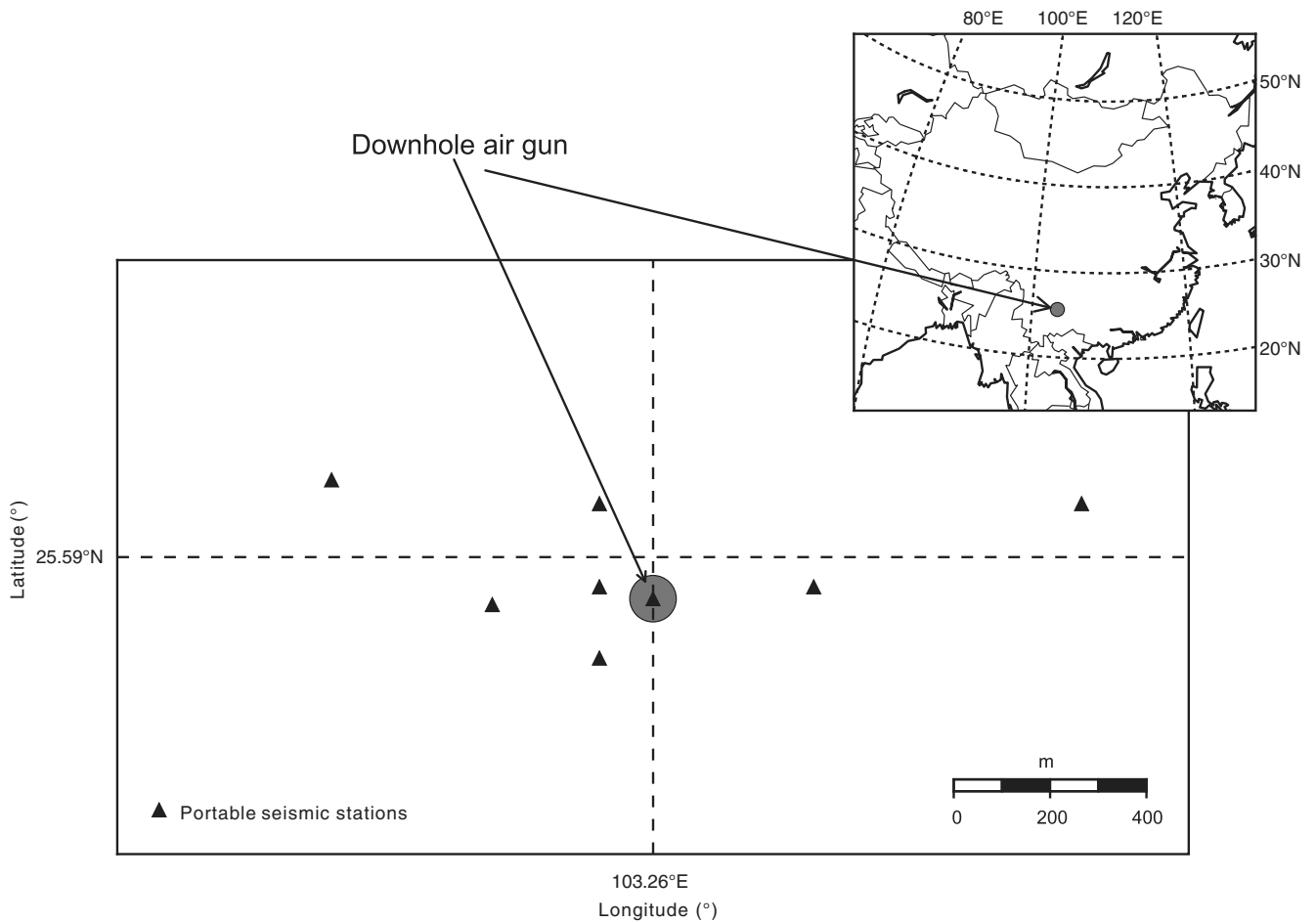

Figure 13. Location of the air-gun source and stations in the Xundian downhole air-gun project. The circle denotes the location of the downhole air-gun source, and the triangles are the stations used in this project. The epicenter distance ranges from approximately 10 to more than 800 m, providing good coverage of the different emergence angles.
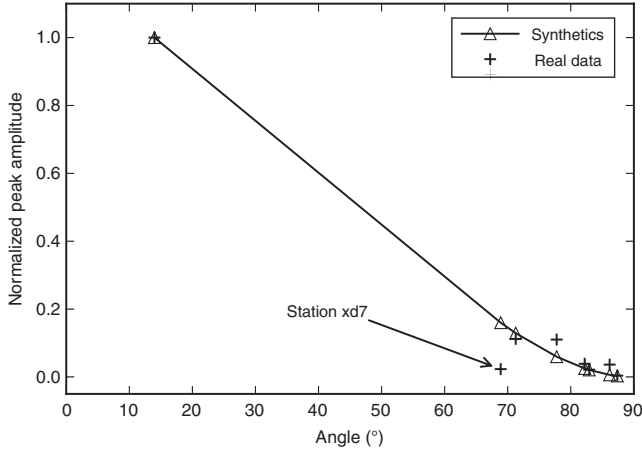
Figure 14. Comparison of the peak amplitude between synthetic seismograms computed by SDI (triangles) and real data from the downhole air-gun project (crosses). Both are normalized by the peak amplitude of the nearest station. The good consistency between them supports the validity of applying a borehole source model to downhole air-gun sources and SDI. The outlier, station xd7, is also found to have significantly lower amplitude for a local earthquake due to unknown reasons, and thus it is excluded from the comparison.

tude with respect to distance because it is difficult to obtain a proper source-time function for a borehole air-gun source. The peak amplitudes of the synthetic seismograms and real data are normalized by the peak amplitude of the nearest station. The result, as shown in Figure 14, demonstrates good coherence between the real and synthetic data. In the borehole source theory, the radiation pattern is dependent on the source-receiver distance and take-off angle. The result shows that the down-hole source model might be suitable for interpretation of amplitude information of a wavefield excited by downhole air-gun sources. However, it is hardly conclusive because the discrepancy between the peak amplitude generated by the borehole source model and the point-source model in the far-field is dominated by spherical spreading. Near-field data are needed in further examinations.

CONCLUSION

We present a new method for computing seismograms of borehole sources, i.e., SDI. An outstanding feature of SDI is that it generates no spurious arrivals. We compare the precision and efficiency of SDI with the classic real-axis integration, and the results show that SDI is more accurate and more efficient when computing far-field seismograms. Additionally, choosing a proper discretization strategy is easier for SDI because of the smoothness and simplicity of the integrand. Experiments in different source-receiver distances demonstrate that SDI is more suitable in far-field cases. However, the Mach-wave example demonstrates that SDI is also applicable to the near-field case. Comparison between synthetic seismograms generated by SDI and real data from a downhole air-gun project also support the validity of our method. Although this method was originally designed for computing seismograms for wavefields excited by borehole sources, it could be extended to other fields in seismology involving highly oscillatory integrals to further improve the efficiency and reduce spurious arrivals.

APPENDIX A

MATHEMATICAL FORMULA OF BOREHOLE SOURCES RADIATION

Theoretically, borehole source models can be divided into two categories, namely, the point-source model and the stress-source model. The point-source model is commonly used in acoustic logging, which consists of monopole, dipole, or quadrupole sources and a fluid-filled borehole. The stress sources are used to describe dynamite sources in deep seismic sounding and mining geophysics, which approximate explosions as stresses acting on the virtual borehole wall. Although arising from different subjects, both models share a similar mathematical formula. Without losing generality, we adopt the stress-source model in this study.

Consider an isotropic linear elastic medium embedded with an empty borehole. The radius of the borehole is denoted by a, and the Lamé parameters and density of the medium are λ, μ, and ρ. First, the analytical solutions in frequency-wavenumber domain are obtained. The equilibrium equation in cylindrical coordinates is

$$
\begin{aligned}
\frac{\partial \sigma_{rr}}{\partial r} + \frac{1}{r}\frac{\partial \sigma_{r\theta}}{\partial \theta} + \frac{\partial \sigma_{rz}}{\partial z} + \frac{\sigma_{rr} - \sigma_{\theta\theta}}{r} &= \rho \frac{\partial^2 u_r}{\partial t^2}, \\
\frac{\partial \sigma_{r\theta}}{\partial r} + \frac{1}{r}\frac{\partial \sigma_{\theta\theta}}{\partial \theta} + \frac{\partial \sigma_{\theta z}}{\partial z} + \frac{2\sigma_{r\theta}}{r} &= \rho \frac{\partial^2 u_\theta}{\partial t^2}, \\
\frac{\partial \sigma_{rz}}{\partial r} + \frac{1}{r}\frac{\partial \sigma_{\theta z}}{\partial \theta} + \frac{\partial \sigma_{zz}}{\partial z} + \frac{\sigma_{rz}}{r} &= \rho \frac{\partial^2 u_z}{\partial t^2}, \quad \text{(A-1)}
\end{aligned}
$$

where $\sigma_{ij}(i, j = r, \theta, z)$ are the stresses, $u_i(I = r, \theta, z)$ are the displacements, and t is the time. Body-force terms are omitted as the gravitational effect is neglected. Together with Hooke's law

$$
\begin{bmatrix}
\sigma_{rr} \\
\sigma_{\theta\theta} \\
\sigma_{zz} \\
\sigma_{\theta z} \\
\sigma_{rz} \\
\sigma_{r\theta}
\end{bmatrix}
=
\begin{bmatrix}
\lambda + 2\mu & \lambda & \lambda & 0 & 0 & 0 \\
\lambda & \lambda + 2\mu & \lambda & 0 & 0 & 0 \\
\lambda & \lambda & \lambda + 2\mu & 0 & 0 & 0 \\
0 & 0 & 0 & \mu & 0 & 0 \\
0 & 0 & 0 & 0 & \mu & 0 \\
0 & 0 & 0 & 0 & 0 & \mu
\end{bmatrix}
\begin{bmatrix}
\varepsilon_{rr} \\
\varepsilon_{\theta\theta} \\
\varepsilon_{zz} \\
2\varepsilon_{\theta z} \\
2\varepsilon_{rz} \\
2\varepsilon_{r\theta}
\end{bmatrix},
$$

$$\text{(A-2)}$$

and the geometric relationship

$$\varepsilon_{rr} = \frac{\partial u_r}{\partial r}, \quad \varepsilon_{\theta\theta} = \frac{u_r}{r} + \frac{1}{r}\frac{\partial u_\theta}{\partial \theta}, \quad \varepsilon_{zz} = \frac{\partial u_z}{\partial z},$$

$$\varepsilon_{r\theta} = \frac{1}{2}\left(\frac{1}{r}\frac{\partial u_r}{\partial \theta} + \frac{\partial u_\theta}{\partial r} - \frac{u_\theta}{r}\right), \quad \varepsilon_{\theta z} = \frac{1}{2}\left(\frac{\partial u_\theta}{\partial z} + \frac{1}{r}\frac{\partial u_z}{\partial \theta}\right),$$

$$\varepsilon_{rz} = \frac{1}{2}\left(\frac{\partial u_z}{\partial r} + \frac{\partial u_r}{\partial z}\right), \tag{A-3}$$

a complete partial differential system of **u** is formed for describing wave propagation in an elastic solid

$$(\lambda+2\mu)\left(\frac{\partial^2 u_r}{\partial r^2} + \frac{1}{r}\frac{\partial u_r}{\partial r}\right) + \frac{\mu}{r^2}\frac{\partial^2 u_r}{\partial \varphi^2} + \mu\frac{\partial^2 u_r}{\partial z^2} - \frac{(\lambda+2\mu)}{r^2}u_r$$
$$+\frac{1}{r}(\lambda+\mu)\frac{\partial^2 u_\theta}{\partial r\partial\theta} - \frac{1}{r^2}(\lambda+3\mu)\frac{\partial u_\theta}{\partial\theta} + (\lambda+\mu)\frac{\partial^2 u_z}{\partial r\partial z} = \rho\frac{\partial^2 u_r}{\partial t^2},$$
$$\frac{1}{r}(\lambda+\mu)\frac{\partial^2 u_r}{\partial r\partial\theta} + \frac{1}{r^2}(\lambda+3\mu)\frac{\partial u_r}{\partial\varphi} + \mu\left(\frac{\partial^2 u_\theta}{\partial r^2} + \frac{1}{r}\frac{\partial u_\theta}{\partial r}\right)$$
$$+\frac{\lambda+2\mu}{r^2}\frac{\partial^2 u_\theta}{\partial\theta^2} + \mu\frac{\partial^2 u_\theta}{\partial z^2} - \frac{\mu}{r^2}u_\theta + \frac{1}{r}(\lambda+\mu)\frac{\partial^2 u_z}{\partial\theta\partial z} = \rho\frac{\partial^2 u_\theta}{\partial t^2},$$
$$(\lambda+\mu)\left(\frac{\partial^2 u_r}{\partial r\partial z} + \frac{1}{r}\frac{\partial u_r}{\partial z}\right) + \frac{1}{r}(\lambda+\mu)\frac{\partial^2 u_\theta}{\partial\theta\partial z}$$
$$+\mu\left(\frac{\partial^2 u_z}{\partial r^2} + \frac{1}{r}\frac{\partial u_z}{\partial r} + \frac{1}{r^2}\frac{\partial^2 u_z}{\partial\varphi^2}\right) + \lambda\frac{\partial^2 u_z}{\partial z^2} = \rho\frac{\partial^2 u_z}{\partial t^2}. \tag{A-4}$$

The boundary conditions are given by assuming an axisymmetric radial source acting on the borehole

$$\sigma_{rr}(r,t)|_{r=a} = \delta(z)G(t),$$
$$\sigma_{r\theta}(r,t)|_{r=a} = 0,$$
$$\sigma_{rz}(r,t)|_{r=a} = 0, \tag{A-5}$$

where $\delta(z)$ is the delta function and $G(t)$ is the source-time function. Similar problems have been studied analytically by Heelan (1953), who consider seismic waves radiated by a finite length of dynamite exploded in a cylindrical blast hole, then by Lee and Balch (1982) for a fluid-filled borehole, and Meredith (1990) and Blair (2007) with semianalytical methods. Despite the various denotations and specific mathematic techniques adopted, they all follow the same idea, that is, constructing the wavefield by superposition of conical waves, and thus they obtain equivalent analytical solutions. To solve this problem, potential functions are used to simplify the equations. The displacement vector **u** can be decomposed into three fields

$$\mathbf{u} = \nabla\phi + \nabla\times[\nabla\chi\mathbf{e}_z + \nabla\times(\psi\mathbf{e}_z)], \tag{A-6}$$

where, χ represent P-, SV-, SH-waves, respectively. Then, the wave equation A-4 can be simplified to

$$\left(\nabla^2-\frac{\partial^2}{\partial z^2}\right)\left\{\left[(\lambda+2\mu)\nabla^2\phi-\rho\frac{\partial^2\phi}{\partial t^2}\right]+\frac{\partial}{\partial z}\left(\mu\nabla^2\psi-\rho\frac{\partial^2\psi}{\partial t^2}\right)\right\}=0,$$
$$\frac{\partial}{\partial z}\left[(\lambda+2\mu)\nabla^2\phi-\rho\frac{\partial^2\phi}{\partial t^2}\right]+\left(\frac{\partial^2}{\partial z^2}-\nabla^2\right)\left(\mu\nabla^2\psi-\rho\frac{\partial^2}{\partial t^2}\psi\right)=0,$$
$$\left(\nabla^2-\frac{\partial^2}{\partial z^2}\right)\left(\mu\nabla^2\chi-\rho\frac{\partial^2\chi}{\partial t^2}\right)=0. \tag{A-7}$$

We assume the potential functions have the following form:

$$\phi(r,z,t) = \left(\frac{1}{2\pi}\right)^2\int_{-\infty}^{+\infty}\int_{-\infty}^{+\infty}f_1 H_n^{(1)}(k_r r)$$
$$\exp(ik_z z - \omega t)dk_z d\omega,$$
$$\psi(r,z,t) = \left(\frac{1}{2\pi}\right)^2\int_{-\infty}^{+\infty}\int_{-\infty}^{+\infty}f_2 H_n^{(1)}(k_r r)$$
$$\exp(ik_z z - \omega t)dk_z d\omega,$$
$$\chi(r,z,t) = \left(\frac{1}{2\pi}\right)^2\int_{-\infty}^{+\infty}\int_{-\infty}^{+\infty}f_3 H_n^{(1)}(k_r r)$$
$$\exp(ik_z z - \omega t)dk_z d\omega, \tag{A-8}$$

where $H_n^{(1,2)}(z)$ are the nth order of the Hankel function of the first or second kind and k_r, k_z are the radial and vertical wavenumbers, respectively. Let $c^{(c,s)}$ be the velocity of P- or S-waves

$$k_r^2 + k_z^2 = \frac{\omega^2}{c^{(c,s)2}}. \tag{A-9}$$

The product of the Hankel and exponential functions represents the conical waves traveling outward, and $f_{1,2,3}$ are the weights of each conical wave. The weights are determined by solving the boundary condition A-5. Finally, the displacements outside the borehole are

$$U_r(r,k_z,\omega) = \frac{k_r^{(c)}(\rho\omega^2 - 2\mu k_z^2)H_1^{(1)}(k_r^{(s)}a)}{D}G(\omega)H_1^{(1)}(k_r^{(c)}r)$$
$$+\frac{2\mu k_r^{(c)}k_z^2 H_1^{(1)}(k_r^{(c)}a)}{D}G(\omega)H_1^{(1)}(k_r^{(s)}r),$$
$$U_z(r,k_z,\omega) = \frac{-ik_z(\rho\omega^2 - 2\mu k_z^2)H_1^{(1)}(k_r^{(s)}a)}{D}G(\omega)H_0^{(1)}(k_r^{(c)}r)$$
$$+\frac{2i\mu k_z k_r^{(c)}k_r^{(s)}H_1^{(1)}(k_r^{(c)}a)}{D}G(\omega)H_0^{(1)}(k_r^{(s)}r), \tag{A-10}$$

where U_r, U_z are the radial and vertical components of displacement in the frequency-wavenumber domain, $k_r^{(c)}$ and $k_r^{(s)}$ are the radial wavenumber associated with P- and S-waves, $G(\omega)$ is the Fourier transform of the source-time function $G(t)$, and D is given by

$$D = (\rho\omega^2 - 2\mu k_z^2)^2 H_0^{(1)}(k_r^{(c)}a)H_1^{(1)}(k_r^{(s)}a)$$
$$+4\mu^2 k_z^2 k_r^{(c)}k_r^{(s)}H_1^{(1)}(k_r^{(c)}a)H_0^{(1)}(k_r^{(s)}a)$$
$$-2\mu\rho\omega^2 k_r^{(c)}\frac{1}{a}H_1^{(1)}(k_r^{(c)}a)H_1^{(1)}(k_r^{(s)}a). \tag{A-11}$$

Then, the solution in the time-space domain is obtained by applying a 2D Fourier transform on the solutions over the vertical wavenumber k_z and the frequency ω.

The dual transform can be evaluated analytically, provided that the radius of borehole a is small compared with the wavelength of interest and the receiver is in the far-field. The solutions then are obtained by asymptotic analysis

$$
u_r(r,z,t) = -\frac{a^2}{4\mu R}\sin\phi\left[\begin{array}{l}\left(1-\frac{2\mu}{\lambda+2\mu}\cos^2\phi\right)\frac{1}{c^{(c)}}G'(t-R/c^{(c)})\\ +2\cos^2\phi\frac{1}{c^{(s)}}G'(t-R/c^{(s)})\end{array}\right],
$$

$$
u_z(r,z,t) = -\frac{a^2}{4\mu R}\cos\phi\left[\begin{array}{l}\left(1-\frac{2\mu}{\lambda+2\mu}\cos^2\phi\right)\frac{1}{c^{(c)}}G'(t-R/c^{(c)})\\ -2\sin^2\phi\frac{1}{c^{(s)}}G'(t-R/c^{(s)})\end{array}\right],
$$

$$\text{(A-12)}$$

where $R(=[(r-a)^2+z^2]^{1/2}\approx(r^2+z^2)^{1/2})$ is the source-receiver distance. This far-field solution is a modified version of the Heelan's (1953) solution. The Heelan's solution has an additional $2\pi l$ factor due to the finite length of the source, while we use a source of infinitesimal length. The far-field solution is used in this study to verify the numerical results under certain conditions.

REFERENCES

Aki, K., and P. G. Richards, 2002, Quantitative seismology: University Science Books.

Blair, D., 2010, Seismic radiation from an explosive column: Geophysics, **75**, no. 1, E55–E65, doi: 10.1190/1.3294860.

Blair, D. P., 2007, A comparison of Heelan and exact solutions for seismic radiation from a short cylindrical charge: Geophysics, **72**, no. 2, E33–E41, doi: 10.1190/1.2424543.

Bouchon, M., 1981, A simple method to calculate Green's functions for elastic layered media: Bulletin of the Seismological Society of America, **71**, 959–971.

Bouchon, M., 2003, A review of the discrete wavenumber method: Pure and Applied Geophysics, **160**, 445–465, doi: 10.1007/PL00012545.

Bouchon, M., and K. Aki, 1977, Discrete wave-number representation of seismic-source wave fields: Bulletin of the Seismological Society of America, **67**, 259–277.

Chen, X., X. Tang, and Y. Qian, 2014, Propagation characteristics of multipole acoustic logging in cracked porous tight formations: Chinese Journal of Geophysics (in Chinese), **57**, 2961–2970.

Chen, X., and H. Zhang, 2001, An efficient method for computing Green's functions for a layered half-space at large epicentral distances: Bulletin of the Seismological Society of America, **91**, 858–869, doi: 10.1785/0120000113.

Cheng, C. H., and M. N. Toksöz, 1981, Elastic wave propagation in a fluid-filled borehole and synthetics acoustic logs: Geophysics, **46**, 1042–1053, doi: 10.1190/1.1441242.

Gradshteyn, I. S., and I. M. Ryzhik, 2007, Table of integrals, series, and products: Academic Press.

He, X., and H. Hu, 2009, Borehole flexural modes in transversely isotropic formations: Low-frequency asymptotic velocity: Geophysics, **74**, no. 4, E149–E158, doi: 10.1190/1.3141442.

Heelan, P. A., 1953, Radiation from a cylindrical source of finite length: Geophysics, **18**, 685–696, doi: 10.1190/1.1437923.

Huybrechs, D., and S. Vandewalle, 2006, On the evaluation of highly oscillatory integrals by analytic continuation: SIAM Journal on Numerical Analysis, **44**, 1026–1048, doi: 10.1137/050636814.

Khanh, B. D., 1995, A numerical evaluation of integrals by the method of steepest descents: Applied Mathematics Letters, **8**, 91–95, doi: 10.1016/0893-9659(94)00117-U.

Kurkjian, A. L., 1985, Numerical computation of individual far-field arrivals excited by an acoustic source in a borehole: Geophysics, **50**, 852–866, doi: 10.1190/1.1441961.

Kurkjian, A. L., and S. Chang, 1986, Acoustic multipole sources in fluid-filled boreholes: Geophysics, **51**, 148–163, doi: 10.1190/1.1442028.

Lee, M. W., and A. H. Balch, 1982, Theoretical seismic wave radiation from a fluid-filled borehole: Geophysics, **47**, 1308–1314, doi: 10.1190/1.1441391.

López, J. L., P. Pagola, and E. P. Sinusía, 2009, A systematization of the saddle point method: Application to the Airy and Hankel functions: Journal of Mathematical Analysis & Applications, **354**, 347–359, doi: 10.1016/j.jmaa.2008.12.032.

Meredith, J. A., 1990, Numerical and analytical modeling of downhole seismic sources: The near and far field: Ph.D. thesis, Massachusetts Institute of Technology.

Meredith, J. A., M. Toksöz, and C. Cheng, 1993, Secondary shear waves from source boreholes: Geophysical Prospecting, **41**, 287–312, doi: 10.1111/j.1365-2478.1993.tb00571.x.

Press, W. H., S. A. Teukolsky, W. T. Vetterling, and B. P. Flannery, 1992, Numerical recipes in C: Cambridge University Press.

Rosenbaum, J. H., 1974, Synthetic microseismograms: Logging in porous formations: Geophysics, **39**, 14–32, doi: 10.1190/1.1440407.

Tang, X., X. Chen, and X. Xu, 2012, A cracked porous medium elastic wave theory and its application to interpreting acoustic data from tight formations: Geophysics, **77**, no. 6, D245–D252, doi: 10.1190/geo2012-0091.1.

Tsang, L., and D. Rader, 1979, Numerical evaluation of the transient acoustic waveform due to a point source in a fluid-filled borehole: Geophysics, **44**, 1706–1720, doi: 10.1190/1.1440932.

Tubman, K. M., C. H. Cheng, and M. N. Toksöz, 1984, Synthetic full waveform acoustic logs in cased boreholes: Geophysics, **49**, 1051–1059, doi: 10.1190/1.1441720.

White, J. E., and R. E. Zechman, 1968, Computed response of an acoustic logging tool: Geophysics, **33**, 302–310, doi: 10.1190/1.1439930.

Xu, Y., T. Xu, M. Wang, Z. Bai, Z. Zhang, and J. Teng, 2015, Far-field wavefield characteristics of downhole seismic sources: Chinese Journal of Geophysics (in Chinese), **58**, 2912–2926, doi: 10.6038/cjg20150824.

Yang, W., B. S. Wang, Z. Y. Liu, J. Yang, X. B. Li, and R. Chen, 2016, Study on the source characteristic of downhole air-gun with different exciting environment: Earthquake Research in China (in Chinese), **32**, 231–240.

Zheng, X., H. Hu, W. Guan, and J. Wang, 2015, Simulation of the borehole quasistatic electric field excited by the acoustic wave during logging while drilling due to electrokinetic effect: Geophysics, **80**, no. 5, D417–D427, doi: 10.1190/geo2014-0506.1.